Sanguinarine chloride inducing ferroptosis and downregulating GPX4 expression in liver cancer: An integrated *in silico*, *in vitro* and *in vivo* study

WEN OUYANG[1*], JIANXIN GAO[1*], JING LIU[1], LULU QIN[2], BANG LIU[1], YING HE[1] and DAI ZHOU[1]

[1]Hunan Provincial Key Laboratory of Regional Hereditary Birth Defect Prevention and Control, Changsha Hospital for Maternal and Child Health Care Affiliated to Hunan Normal University, Changsha, Hunan 410000, P.R. China; [2]Health Science Center, School of Public Health, Hunan Normal University, Changsha, Hunan 410081, P.R. China

Received May 15, 2026; Accepted July 22, 2026

DOI: 10.3892/etm.2026.13266

Abstract. Ferroptosis, an iron-dependent form of regulated cell death driven by excessive lipid peroxidation, has been increasingly implicated in the development and progression of liver cancer. Despite sanguinarine chloride (SC) exhibiting antitumor activity in a number of cancer models, whether it modulates ferroptosis in liver cancer remains unclear. The present study systematically investigated the ferroptosis-inducing effects of SC and the underlying molecular mechanisms in liver cancer. Molecular docking and molecular dynamics simulations suggested that SC interacts with glutathione peroxidase 4 (GPX4) with favorable affinity and forms a stable complex. Functional assays showed that SC significantly inhibited proliferation and reduced the viability of HepG2 and Huh7 cells. Mechanistically, SC markedly decreased GPX4 protein expression, leading to the accumulation of lipid reactive oxygen species and malondialdehyde, together with characteristic mitochondrial changes associated with ferroptosis, including increased membrane density and loss of cristae. SC-induced cell death was partially rescued by the ferroptosis inhibitors ferrostatin-1 and deferoxamine, further supporting the involvement of ferroptosis. Consistently, in a xenograft model, SC suppressed GPX4 expression, promoted ferroptosis and significantly inhibited tumor growth. Collectively, these findings indicate that SC exerts antitumor effects in liver cancer, at least in part, by inducing ferroptosis through GPX4 downregulation, supporting further investigation of SC as a potential therapeutic candidate.

Correspondence to: Dr Ying He or Dr Dai Zhou, Hunan Provincial Key Laboratory of Regional Hereditary Birth Defect Prevention and Control, Changsha Hospital for Maternal and Child Health Care Affiliated to Hunan Normal University, 416 Chengnan Road, Changsha, Hunan 410000, P.R. China
E-mail: 1048774424@qq.com
E-mail: zhoudai@hunnu.edu.cn

*Contributed equally

Key words: sanguinarine chloride, liver cancer, ferroptosis, glutathione peroxidase 4

Introduction

Primary liver cancer is among the most common malignancies worldwide, ranking sixth in global incidence (4.3%) and third in cancer-associated mortality (7.8%) (1). According to Global Cancer Observatory estimates, ~865,269 new liver cancer cases and 757,948 associated mortalities occur annually. China bears a disproportionately high burden of liver cancer because of its high disease incidence and large population. Despite notable advances in treatment, including surgical resection, transarterial chemoembolization and radiofrequency ablation, key clinical challenges remain, such as treatment-associated toxicity, drug resistance and poor outcomes in patients with advanced disease (2-6). Therefore, more effective and well-tolerated therapeutic strategies are urgently needed.

Natural bioactive compounds have drawn widespread attention due to their potent pharmacological effects and low systemic toxicity (7-17). Sanguinarine chloride (SC), a benzophenanthridine alkaloid primarily derived from the roots of *Sanguinaria canadensis*, seeds of *Argemone* mexicana and the leaves and fruits of *Macleaya* cordata, is among the most extensively studied compounds in this class (9-14). Accumulating *in vitro* and *in vivo* investigations have verified that SC exerts broad-spectrum anti-tumor activities across various malignancies, including antioxidant, anti-inflammatory, pro-apoptotic and anti-proliferative effects (9-14). Existing literature has also documented that SC triggers apoptosis and ferroptosis, represses angiogenesis and attenuates the invasive capacity of tumor cells. However, its functional phenotypes, direct molecular targets and detailed regulatory mechanisms specific to liver cancer remain poorly characterized. Accordingly, the present study was conducted to systematically assess the anti-tumor potency of SC and investigate its underlying molecular cascades in liver cancer.

Ferroptosis is an iron-dependent form of regulated cell death characterized by the lethal accumulation of lipid reactive

oxygen species (ROS) and has attracted marked interest in oncology (18-22). Inhibition or inactivation of glutathione peroxidase 4 (GPX4) causes lipid peroxide accumulation and triggers ferroptosis (18). This mechanistic insight has prompted the development of pharmacological strategies targeting GPX4 as a potential approach to cancer treatment (19-22). A number of small molecules, including RAS-selective lethal 3 (RSL3), have been identified as direct GPX4 inhibitors and are widely used as experimental tools for studying this pathway (20). However, their clinical translation is limited by potential off-target effects, chemical instability, cell-type-dependent activity, non-specific cytotoxicity, formulation and delivery challenges, insufficient validation in physiologically relevant models and the absence of clinical approval (21,23). Therefore, identifying new, well-tolerated agents that induce ferroptosis through the GPX4 axis remains an important objective in liver cancer therapy.

The present study first verified that SC exerts notable suppressive effects on the proliferation of HepG2 and Huh7 cell lines. The potential molecular targets and underlying mechanisms of SC in these two cellular models were then further explored. To systematically address this question, a multi-dimensional experimental strategy was employed, encompassing: i) Quantification detection of ROS and malondialdehyde (MDA, two key biochemical markers of ferroptosis; ii) transmission electron microscopy (TEM) observations to assess ultra-structural changes characteristic of ferroptosis (such as shrunken mitochondria with decreased cristae); iii) molecular docking simulations to predict the binding mode and affinity between SC and core ferroptosis-associated proteins; iv) molecular dynamics (MD) simulations to evaluate the stability of the SC-protein complex over time; v) western blot analysis to detect changes in the expression levels of GPX4 and; vi) *in vivo* xenograft tumor assays to validate the anti-liver cancer therapeutic efficacy of SC. To the best of our knowledge, this study is the first to uncover the regulatory linkage between the natural compound SC and the core ferroptosis mediator GPX4 in liver cancer, offering novel mechanistic evidence for developing natural small-molecule targeted therapies against liver cancer.

Materials and methods

Reagents and cell culture. SC was purchased from Shanghai Aladdin Biochemical Technology Co., Ltd. It was initially dissolved in DMSO to create a 10 mM stock solution and subsequently diluted with culture medium to the desired working concentrations. HepG2 cells were obtained from the Cell Bank of the Chinese Academy of Sciences (cat. no. SCSP-510). Huh7 cells were purchased from Shanghai Zhong Qiao Xin Zhou Biotechnology Co., Ltd. (cat. no. ZQ0025; https://www.zqxzbio.com/Index/p_more/pid/478.html). HepG2 and Huh7 were employed for subsequent *in vitro* functional assays and were maintained in DMEM supplemented with 10% FBS (Wuxi NEST Biotechnology Co., Ltd.) and 100 U/ml penicillin and 100 μg/ml streptomycin. Cells were cultured in a humidified incubator at 37˚C with 5% CO_2. Both cell lines were routinely tested and confirmed to be free of *Mycoplasma* contamination.

Cell viability and rescue assays. Cell viability was assessed using a Cell Counting Kit-8 (CCK-8; Shandong Topscience Biotech Co., Ltd.). Briefly, HepG2 and Huh7 cells were seeded in 96-well plates at a density of $5x10^4$ cells/well and incubated overnight at 37˚C with 5% CO_2. For dose-response analysis, cells were treated with increasing concentrations of SC (0, 1, 2, 5, 10 and 20 μM) for 48 h at 37˚C. For rescue assays, cells were co-treated with SC (2 μM) and either ferrostatin-1 (Fer-1; 20 μM) or deferoxamine (DFO; 50 μM) for 48 h. Subsequently, 10 μl CCK-8 solution was added to each well and the plates were incubated for an additional 1-2 h. Absorbance at 450 nm was measured using the EnSpire PerkinElmer microplate reader.

Cell morphology and TEM. To examine ultrastructural changes, HepG2 and Huh7 cells were seeded in 10-cm dishes and treated with the indicated concentrations of SC. After treatment, both adherent and detached cells were collected and centrifuged at $1.5093x10^3$ x g for 5 min at 4˚C. Cell pellets were fixed in 2.5% glutaraldehyde for 2 h at 4˚C, washed three times with PBS and postfixed in 1% osmium tetroxide at 4˚C. Samples were then dehydrated through a graded ethanol series (30 to 100%). Ultrathin sections (60-80 nm) were prepared using an ultramicrotome, double-stained with 2% uranyl acetate and lead citrate at room temperature for 15 min and imaged using an HT7700 transmission electron microscope (Hitachi, Ltd.).

Assessment of lipid ROS and MDA levels. Lipid ROS and MDA levels in HepG2 and Huh7 cells were assessed after 48 h of treatment. Cellular lipid ROS levels were measured using C11-BODIPY 581/591 (cat. no. GC40165; GlpBio Technology) according to the manufacturer's instructions, with SC-treated cells compared with DMSO vehicle controls. MDA levels were quantified using a commercial MDA assay kit (cat. no. A003-1-2; Nanjing Jiancheng Bioengineering Institute) according to protocol's instructions, with SC-treated cells compared with DMSO vehicle controls. Each experiment was performed with at least three biological replicates.

Colony formation assay. Clonogenic capacity of cells was assessed using a colony formation assay. HepG2 and Huh7 cells were seeded in 6-well plates at a density of 600 cells/well. After 24 h of attachment, cells were treated with SC (0, 1 or 2 μM) at 37˚C. After 7 days, the medium was removed and the cells were washed three times with PBS. Colonies were fixed with 4% paraformaldehyde for 15 min at room temperature and stained with 1% crystal violet for 15 min at room temperature. The plates were then washed with ultrapure water, air-dried and photographed. Colonies (defined as containing >50 cells) were manually counted.

Molecular docking. Molecular docking was performed to investigate interactions between SC and ferroptosis-associated proteins. The three-dimensional structure of SC was obtained from PubChem (https://pubchem.ncbi.nlm.nih.gov/compound/68635) and the protein structures were downloaded from the Research Collaboratory for Structural Bioinformatics Protein Data Bank (https://www.rcsb.org/structure/2GS3). Before docking, the ligand structure

was energy-minimized using Avogadro (https://avogadro.cc; version 2.0). Docking simulations were performed using AutoDock Vina (https://ccsb.scripps.edu/adfr/; version 1.0) and binding sites were defined using AutoDockTools (version 2.0). The exhaustiveness parameter was set to 100. The resulting complexes were analyzed for hydrogen-bonding and other interactions and visualized using PyMOL (https://www.pymol.org/pymol.html; version 3.1).

MD simulations. *MD* simulations were performed using GROMACS (version 2020.1). Topology files for small molecules were generated using the LigParGen server (https://traken.chem.yale.edu/ligpargen/) and the 'CHARMM36' force field was applied to both proteins and ligands. Each system was solvated in a dodecahedral box with a 10 Å buffer using the TIP3P water model and neutralized with 35 Na^+ and 27 Cl^- ions to achieve a physiological salt concentration of 0.15 M.

Energy minimization was performed using the steepest-descent algorithm for 10,000 steps. This was followed by 10 ns of equilibration under the NVT ensemble (constant number of atoms, volume and temperature) at 310 K and a 100 ns production simulation under the constant number of particles, pressure and temperature ensemble at 310 K and 1 atm. Bond lengths were constrained using the Linear Constraint Solver algorithm. A 2 fs integration time step was used, with a 1.2 nm cut-off for both Coulomb and van der Waals interactions. Long-range electrostatic interactions were calculated using the particle mesh Ewald method (24).

Independent 100 ns simulations were performed for apo-GPX4 and the GPX4-ligand complex with the lowest docking energy. Trajectories were analyzed for hydrogen bonding, root mean square deviation (RMSD), solvent-accessible surface area (SASA), radius of gyration (Rg) and root mean square fluctuation (RMSF). Binding free energy was estimated using the molecular mechanics Poisson-Boltzmann surface area (MM-PBSA) method implemented in the 'g_mmpbsa' tool.

Prediction of absorption distribution metabolism excretion (ADME) and drug-likeness properties of SC. ADME prospects and drug-likeness properties of SC were predicted using ADMETlab version 2.0 (https://admetmesh.scbdd.com/service/evaluation/index) and SwissADME (http://www.swissadme.ch/index.php) tool. The SMILES sequence of SC was initially retrieved from the PubChem database (https://pubchem.ncbi.nlm.nih.gov/) and subsequently inputted into the database, resulting in the retrieval of the predicted results.

Measurement of GPX4 activity. GPX4 activities were measured using the respective Speedy™ Human GPX4 One-Step ELISA Kit (cat. no. SE50108-96T; Proteintech Group, Inc.). Briefly, cells were cultured in 10 cm^2 plates overnight and treated with DMSO, 1 and 2 μM SC for 48 h at 37˚C. After treatments, cells were washed with PBS and collected to measure intracellular GPX4 activity in accordance with the manufacturer's instructions.

Western blot analysis. HepG2 and Huh7 cells were lysed in RIPA buffer (cat. no. P0013VS; Beyotime Biotechnology) supplemented with protease inhibitors. Protein concentrations were determined using a BCA Protein Assay Kit (cat. no. P0011; Beyotime Biotechnology). Equal amounts of protein (30 μg) were separated by SDS-PAGE and transferred to PVDF membranes. After blocking with 5% non-fat milk in Tris-buffered saline with 0.05% Tween-20 (TBST) for 1 h at room temperature, the membranes were incubated overnight at 4˚C with primary antibodies against GPX4 (cat. no. AFRM0237; 1:1,000; Hunan Aifang Biological Co., Ltd.) and β-tubulin (cat. no. 10094-1-AP; 1:5,000; Proteintech Group, Inc.). After washing with TBST (0.05% Tween-20), the membranes were incubated with the appropriate HRP-conjugated Goat Anti-Rabbit IgG (H+L) secondary antibodies (cat. no. A21220; 1:10,000; Abbkine Scientific Co., Ltd.) for 1 h at room temperature. Protein bands were visualized using an ECL Prime Western Blotting Detection Kit (cat. no. BMP3010; Abbkine Scientific Co., Ltd.).

In vivo mouse study. Experimental protocols were approved by the Ethics Committee for Biomedical Research of Hunan Normal University (approval no. 20250908). All mice were housed under specific pathogen-free conditions with a controlled environment (temperature: 20-25˚C; humidity: 50-60%) and a 12-h light/dark cycle. Animals were provided with a standard rodent diet and water *ad libitum*. HepG2 cells ($2x10^6$ cells in 100 μl PBS/Matrigel mixture; 1:1; v/v) were subcutaneously injected into the flanks of nude mice. When tumor volumes reached ~100 mm^3, the mice were randomly assigned to two experimental groups (n=5 per group). A total of 10 mice bearing established HepG2 tumors (mean volume: ~100 mm^3) were randomly assigned to two groups: A vehicle control group and an SC treatment group. SC was formulated in a vehicle containing 5% DMSO, 10% polyethylene glycol 300, 1% Tween-80 and 84% saline and administered intravenously at 5 mg/kg every 2 days. Tumor dimensions were measured every 2 days using digital calipers and tumor volume was calculated as follows: volume=length x $width^2/2$. On day 14, all animals were euthanized. No mice met the predefined humane endpoints, defined as ≥20% body weight loss or moribund status. At the experimental endpoint, euthanasia was performed by intraperitoneal injection of pentobarbital sodium (50 mg/kg) followed by cervical dislocation. Mortality was determined by visual confirmation of cardiac and respiratory arrest. At the present study endpoint, tumors were excised, weighed and subjected to immunohistochemical (IHC) staining to assess GPX4 expression.

IHC staining. Mouse tumor specimens were fixed with a 4% paraformaldehyde solution at room temperature for 24 h, followed by paraffin embedding and serial sectioning (thickness, 4 μm). For IHC staining, the sections were rehydrated and antigen retrieval was performed in high-temperature citric acid solution at 160˚C for 10 min and washed with PBS. Sections were blocked with 3% H_2O_2 at room temperature for 10 min, followed by blocking with PBS containing 5% BSA at room temperature for 30 min. Primary GPX4 antibodies (cat. no. AFRM0237; 1:1,000; Hunan Aifang Biological Co., Ltd.) were added at 4˚C in the dark overnight. The sections were incubated with a universal secondary antibody (HRP-conjugated goat anti-mouse/rabbit IgG;

cat. no. TBAG0036; Wuhan Servicebio Technology Co., Ltd.) at a dilution of 1:200 at room temperature for 1 h. DAB substrate chromogen (cat. no. G1212-200T; Wuhan Servicebio Technology Co., Ltd.) was added for 20 min. For nuclear counterstaining, the sections were stained with hematoxylin at room temperature for 1-2 min. The sections were observed and images were captured using a light microscope (magnification, x100 and x400; OLYMPUS IX73; Olympus Corporation) and analyzed using ImageJ software (version 1.8.0; National Institutes of Health).

Statistical analysis. Quantitative data are presented as the mean ± SEM. Data were assessed for normality and homogeneity of variance before statistical testing. Comparisons between two groups were performed using an unpaired, two-tailed Student's t-test, whereas comparisons among multiple groups were performed using one-way ANOVA. A two-sided $P<0.05$ was considered to indicate a statistically significant difference. Statistical analyses were performed using GraphPad Prism (version 10.0; Dotmatics). Statistical significance is indicated in the figures as follows: $^{*}P<0.05$, $^{**}P<0.01$, $^{***}P<0.001$ and $^{****}P<0.0001$.

Results

SC inhibits liver cancer cell viability and clonogenic growth. To assess the antiproliferative effects of SC, a CCK-8 assay was used to measure the viability of HepG2 and Huh7 cells. Resulting dose-response curves are shown in Fig. 1A and B. After 48 h of treatment, SC significantly reduced the viability of both cell lines in a concentration-dependent manner. The IC_{50} values of SC in HepG2 and Huh7 cells were 3.099 and 2.796 μM, respectively. Colony formation assays further showed that SC significantly reduced clonogenic growth in both cell lines in a concentration-dependent manner (Fig. 1C). These results demonstrated that SC suppressed the viability and clonogenic growth of liver cancer cells.

SC induces ferroptosis in liver cancer cells. To determine whether ferroptosis contributes to SC-induced cell death, HepG2 and Huh7 cells were treated with SC alone or in combination with the ferroptosis inhibitors Fer-1 or DFO. In HepG2 cells, SC treatment alone was shown to significantly reduce cell viability compared with the Fer-1 or DFO alone, whereas co-treatment with either Fer-1 or DFO partially restored this viability relative to SC treatment alone (Fig. 2A and B). A similar rescue effect was observed in Huh7 cells (Fig. 2C and D). These findings support the involvement of ferroptosis in SC-induced death of liver cancer cells.

To obtain biochemical and ultrastructural evidence of ferroptosis, lipid ROS and MDA levels were measured and mitochondrial morphology was examined. Fluorescence microscopy revealed an increase in C11-BODIPY (an oxidation-sensitive fluorescent fatty acid analogue) oxidation in SC-treated HepG2 and Huh7 cells (Fig. 3A and B), with quantitative analysis demonstrating significant lipid ROS accumulation (Fig. 3C and D). MDA levels were also found to be significantly increased after SC treatment in both cell lines (Fig. 3E and F). Morphological examination revealed no prominent apoptotic features, such as membrane blebbing or chromatin condensation. Instead, TEM showed ferroptosis-associated mitochondrial alterations, including increased membrane density and loss of cristae (Fig. 4). Together, these biochemical and ultrastructural findings supported the induction of ferroptosis by SC in HepG2 and Huh7 cells.

SC downregulates GPX4 and induces ferroptosis. To identify potential ferroptosis-associated targets of SC, molecular docking simulations were performed. SC exhibited favorable predicted binding affinities for a number of ferroptosis regulators, including GPX4 (-7.50 kcal/mol), long-chain acyl-CoA synthetase 4 (-7.43 kcal/mol), ferritin light chain (-6.65 kcal/mol), ferritin heavy chain (-6.44 kcal/mol), six-transmembrane epithelial antigen of prostate 3 (-7.19 kcal/mol), solute carrier family 3 member 2 (-6.14 kcal/mol), solute carrier family 7 member 11 (-7.20 kcal/mol) and solute carrier family 1 member 5 (-6.65 kcal/mol).

GPX4 is a key glutathione peroxidase that suppresses ferroptosis (25-29). Molecular docking predicted a favorable interaction between SC and GPX4, with a binding energy of -7.50 kcal/mol. The docked GPX4-SC complex contained five hydrophobic and five non-bonded interactions (Fig. 5A and B). SC formed a hydrogen bond with LYS58 and van der Waals interactions with Met129, Phe127, Val54, Ile49 and Ala121. In addition, pi-cation interactions were predicted with Lys117 and Asp50 and pi-anion interactions with Asp48 and Asp128. GPX4 protein expression was next examined by western blotting. SC treatment significantly reduced GPX4 protein levels in both HepG2 and Huh7 cells compared with vehicle-treated controls (Fig. 5C). The effect of SC on GPX4 enzymatic activity was evaluated in HepG2 and Huh7 cells. As presented in Fig. 5D, treatment with SC resulted in a significant reduction in GPX4 activity in both hepatocellular carcinoma cell lines. Together, these *in silico* and experimental findings suggested that GPX4 downregulation was associated with SC-induced ferroptosis in liver cancer cells.

To evaluate the stability and dynamics of the SC-GPX4 complex, MD simulations were performed. The SC-GPX4 complex exhibited an average RMSD of 1.6 Å, indicating overall structural stability during the simulation (Fig. 6A). The Rg remained below 15 Å throughout the simulation, suggesting minimal changes in protein compactness and conformational integrity (Fig. 6B). SASA exhibited moderate fluctuations consistent with local ligand-induced changes in solvent exposure (Fig. 6C). A single stable hydrogen bond was maintained throughout the 100 ns simulation, indicating a persistent interaction between SC and GPX4 (Fig. 6D). RMSF analysis showed generally low residue flexibility in the presence of SC (Fig. 6E). Principal component and free-energy landscape analyses identified one intermediate state and one dominant deep-energy basin, suggesting a predominant, stable binding conformation (Fig. 6F). MM-PBSA analysis yielded a binding free energy of -16.32 kcal/mol (Fig. 6G), with major contributions from Met129, Val125, Ala121, Lys117, Ala120 and Ile49 (Fig. 6H). Overall, the MD simulations supported a stable interaction between SC and GPX4.

ADME and drug-likeness properties of SC: An in silico prediction. SC possessed well-balanced counts of hydrogen bond donors, hydrogen bond acceptors, rotatable bonds,

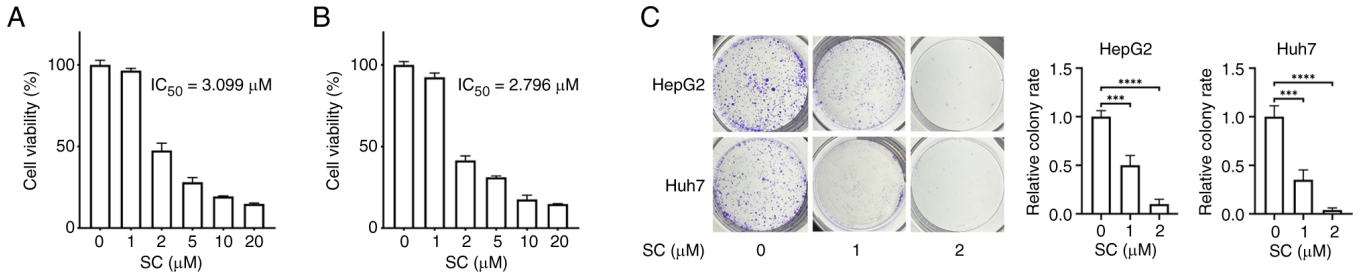

Figure 1. Effects of SC on liver cancer cell viability and clonogenic growth. Viability of (A) HepG2 and (B) Huh7 cells after treatment with increasing concentrations of SC (n=3). (C) Colony formation of HepG2 and Huh7 cells treated with SC (n=3). ***P<0.001 and ****P<0.0001. SC, sanguinarine chloride.

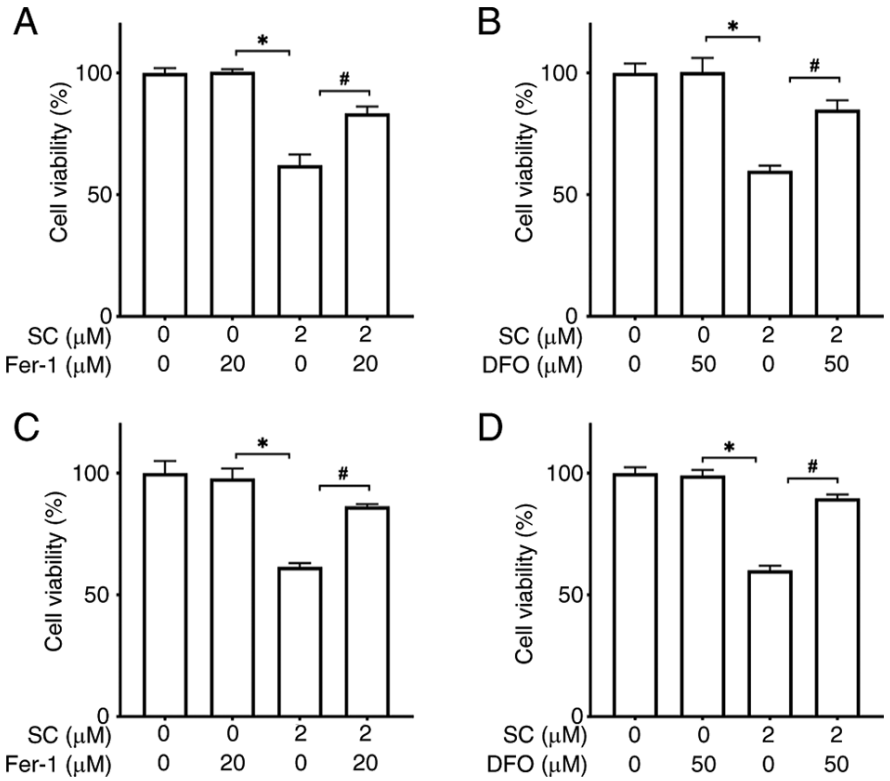

Figure 2. Ferroptosis inhibitors partially rescue SC-induced cytotoxicity. Viability of HepG2 cells treated with SC in the presence or absence of (A) Fer-1 or (B) DFO. Viability of Huh7 cells treated with SC in the presence or absence of (C) Fer-1 or (D) DFO (n=3). *P<0.05 vs. control and #P<0.05 vs. SC alone. SC, sanguinarine chloride; Fer-1, ferrostatin-1; DFO, deferoxamine.

heteroatoms and heavy atoms, satisfying classic thresholds for standard molecular descriptors and drug-likeness criteria. *In silico* absorption simulations predicted favorable gastrointestinal absorption for SC, accompanied by robust Caco-2 permeability with an apparent permeability value of -5.042, moderate MDCK permeability at $5.7x10^{-5}$ cm/s, moderate human intestinal absorption and an estimated oral bioavailability of 20%.

Notably, SC exhibited minimal inhibitory activity against core cytochrome P450 isoforms, namely Cyp2C9, Cyp2C19, Cyp2D6 and Cyp3A4, implying low risk of metabolic drug-drug interactions. Further pharmacokinetic distribution assessments demonstrated promising tissue distribution behavior: SC exhibited moderate plasma protein binding (84.06%), a relatively large steady-state volume of distribution (1.433 l/kg) and theoretical capability to penetrate the blood-brain barrier. In addition, SC fully passed five mainstream drug-likeness filters, including Lipinski's Rule of Five, Ghose's filter, Veber's rule, Egan's filter and Muegge's filter. It displayed a medium elimination half-life >3 h and attained a bioavailability score of 0.55 (Fig. S1).

SC induces ferroptosis and exerts antitumor effects in vivo. *In vitro* results indicated that SC induces ferroptosis in liver cancer cells. To evaluate its antitumor activity *in vivo*, a subcutaneous HepG2 xenograft model was established (Fig. 7A). When the mean tumor volume reached ~100 mm^3, the mice were randomly assigned to a control group or an SC treatment group and received SC at 5 mg/kg as aforementioned.

SC markedly suppressed tumor growth *in vivo* (Fig. 7B). Body weight did not differ significantly between the control and SC-treated groups (Fig. 7C). Plasma alanine aminotransferase

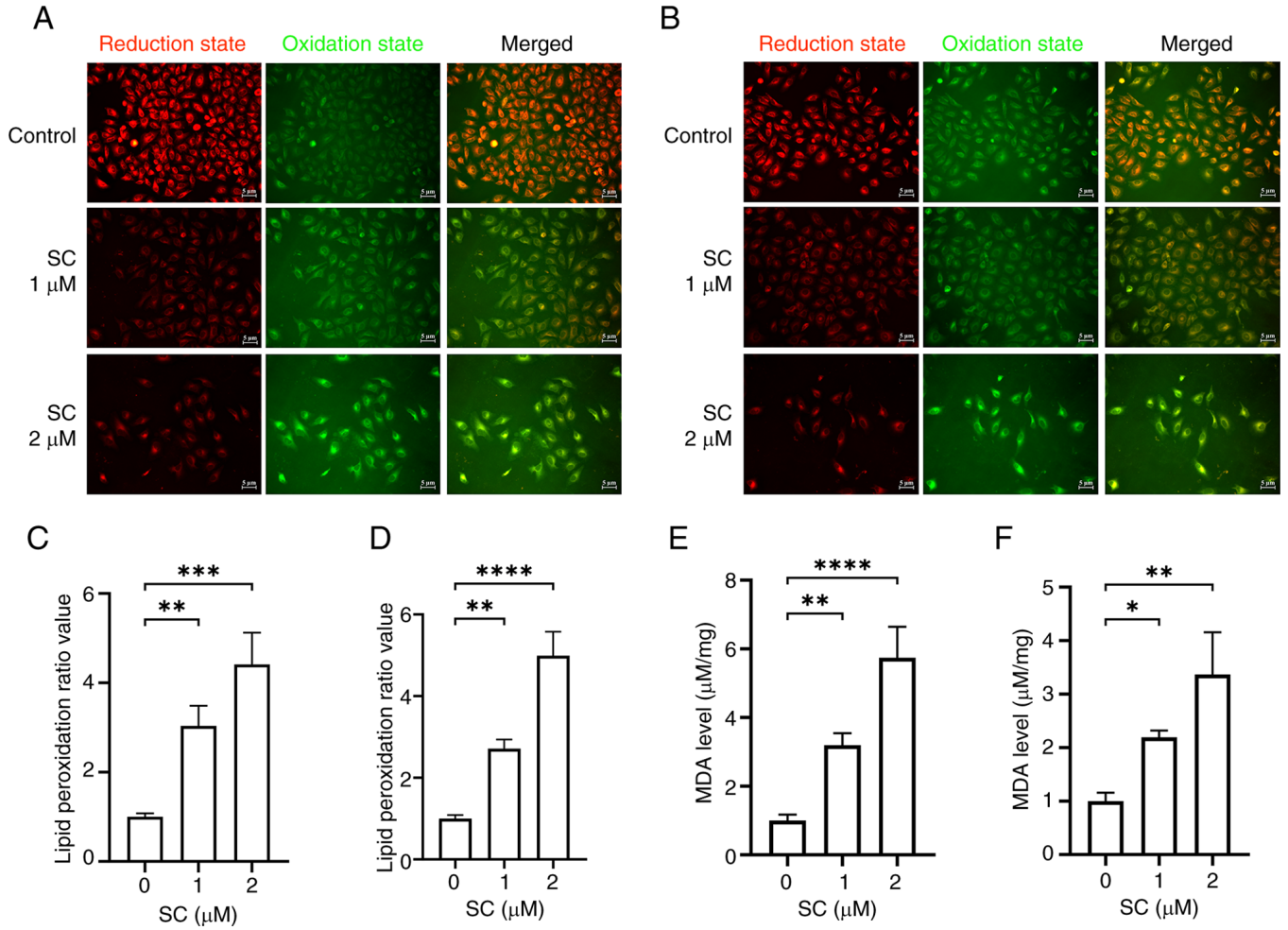

Figure 3. SC increases lipid ROS and MDA levels in liver cancer cells. Representative C11-BODIPY 581/591 fluorescence images of (A) HepG2 and (B) Huh7 cells after SC treatment (scale bar, 5 μm). Quantification of lipid ROS in (C) HepG2 and (D) Huh7 cells after SC treatment (n=3). MDA levels in (E) HepG2 and (F) Huh7 cells after SC treatment (n=3). *P<0.05, **P<0.01, ***P<0.001 and ****P<0.0001. SC, sanguinarine chloride; ROS, reactive oxygen species; MDA, malondialdehyde.

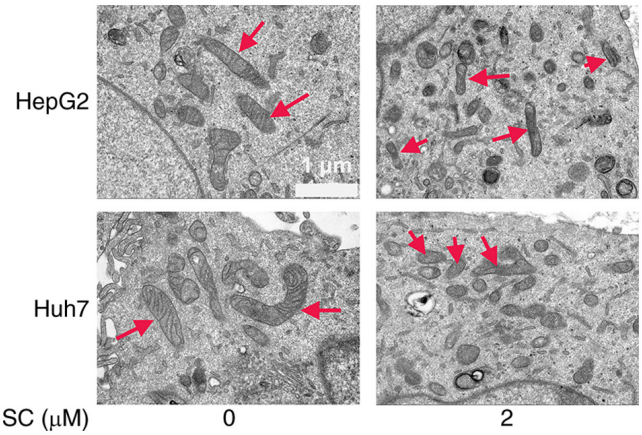

Figure 4. Representative transmission electron microscope images of HepG2 and Huh7 cells treated with DMSO (left) or SC (2 μM; right). Red arrowheads indicate mitochondria. Scale bar = 1 μm. DMSO, dimethyl sulfoxide; SC, sanguinarine chloride.

and aspartate aminotransferase levels also remained comparable between groups (Fig. 7D and E), suggesting no detectable hepatotoxicity under the experimental conditions.

Tumor weight was significantly lower in the SC-treated group compared with the control group at the endpoint (Fig. 7F). Tumor volume was also reduced throughout the treatment period, with a significant difference observed on day 14 (Fig. 7G and H). These findings demonstrated that SC exerted notable antitumor activity in the HepG2 xenograft model.

To determine whether the *in vivo* antitumor effects of SC were associated with ferroptosis, ferroptosis-associated markers were analyzed in resected tumor tissues. Consistent with the cellular findings, SC treatment significantly increased MDA levels (Fig. 7I). IHC staining further exhibited significantly reduced expression of GPX4, a key negative regulator of ferroptosis, in tumors from the SC-treated group compared with the control group (Fig. 7J). These findings indicated that the *in vivo* antitumor effects of SC were associated with GPX4 downregulation and ferroptosis induction in HepG2-derived xenografts.

Discussion

GPX4 is a central suppressor of ferroptosis that uses glutathione to detoxify phospholipid hydroperoxides and protect cells from ferroptosis death (25-34). In liver cancer,

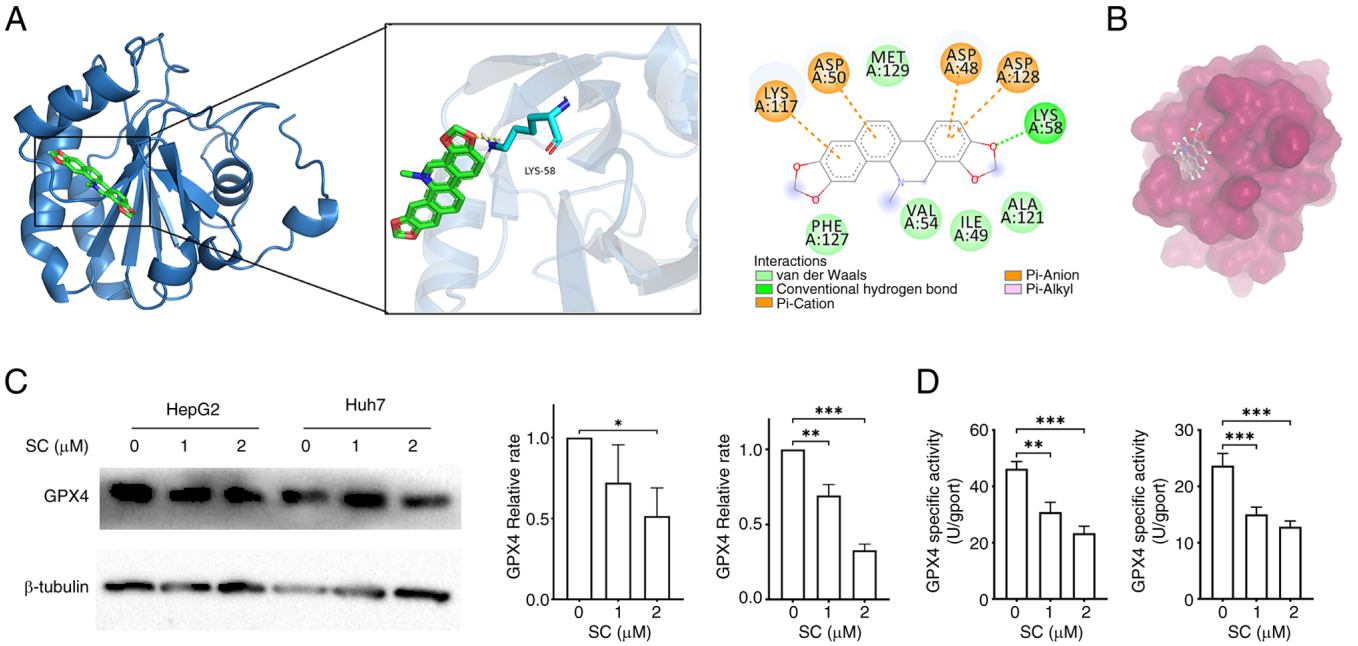

Figure 5. SC downregulates GPX4 in liver cancer cells. (A) Two-dimensional representation of predicted SC-GPX4 interactions. (B) Molecular docking model showing the predicted binding conformation of SC within GPX4. (C) Representative western blots (left) and quantitative analysis (right) of GPX4 protein expression in HepG2 and Huh7 cells after SC treatment (n=3). (D) Activity of GPX4 was detected in the HepG2 (left) and Huh7 (right) cells after treatment with SC. *P<0.05, **P<0.01 and ***P<0.001. SC, sanguinarine chloride; GPX4, glutathione peroxidase 4.

GPX4 has been reported to promote metastasis through transcriptional repression of GRHL3 and activation of the PTEN/PI3K/Akt pathway (28). The long noncoding RNA linc01134, the upregulation of which is associated with poor clinical outcomes in liver cancer, recruits Nrf2 to the GPX4 promoter and increases GPX4 transcription. Inhibition of linc01134 has been shown to increase lipid ROS and MDA accumulation, reduce the glutathione/glutathione disulfide ratio and sensitize liver cancer cells to oxaliplatin by promoting ferroptosis (32). In radioresistant liver cancer, tripartite motif (TRIM)-14-mediated recruitment of ubiquitin-specific protease 14 (USP14) stabilizes GPX4; disruption of the TRIM14/USP14 axis promotes GPX4 degradation and enhances the response to radiotherapy (34). Targeting the TRIM34-associated GPX4 regulatory pathway has also been shown to increase ferroptosis sensitivity and improve immunotherapy efficacy in liver cancer (33). Despite evidence associating GPX4 with liver cancer progression and treatment resistance, the clinical development of canonical GPX4 inhibitors, including RSL3, ML162 and FIN56, remains limited by off-target toxicity, poor chemical stability, cell-type-dependent effects, formulation challenges, insufficient preclinical validation and the absence of clinical approval (21,23). These limitations underscore the need to identify new and potentially more well-tolerated agents that modulate the GPX4-ferroptosis axis in liver cancer.

SC has demonstrated anticancer activity across multiple cancer cell lines (10-14); however, its association with GPX4 in liver cancer remains poorly understood. In the present study, molecular docking and MD simulations predicted a favorable and stable interaction between SC and GPX4. Consistent with the reported upregulation of GPX4 in liver cancer tissues (27), the present western blotting results showed that SC significantly reduced GPX4 protein levels in HepG2 and Huh7 cells. In addition, Fer-1 and DFO partially rescued the reduction in cell viability caused by SC, providing functional evidence that ferroptosis contributes to its cytotoxic effects. In the xenograft model, SC also decreased GPX4 expression and inhibited tumor growth. Collectively, these results suggest that SC induces ferroptosis in liver cancer cells in association with GPX4 downregulation. As a naturally derived benzophenanthridine alkaloid, SC may provide a useful lead scaffold for the development of ferroptosis-inducing therapies. However, the computational evidence presented here does not establish direct target engagement and the pharmacological selectivity and safety of SC require further investigation. Ki-67 and TUNEL staining were not performed in the present study, limiting the assessment of proliferation and apoptosis *in vivo*. In addition, GPX4 overexpression rescue experiments are needed to establish a direct causal association between GPX4 downregulation and SC-induced ferroptosis.

Beyond ferroptosis induction, accumulating evidence (10-14) has demonstrated that SC modulates multiple regulated cell death pathways, including apoptosis, necroptosis and proptosis, which may jointly contribute to its anti-liver cancer activity. The present study primarily focused on characterizing the ferroptosis-triggering effect of SC, as the present phenotypic verification using Fer-1 and DFO rescue experiments demonstrated that ferroptosis serves as a dominant effector pathway mediating SC-induced tumor suppression. However, the potential auxiliary involvement of apoptosis or other RCD subtypes in SC-mediated anti-tumor outcomes cannot be ruled out. Concurrent activation of apoptotic signaling may synergize with lipid peroxidation-driven ferroptosis to amplify the growth-inhibitory effect on liver cancer cells. Future systematic investigations, including combined

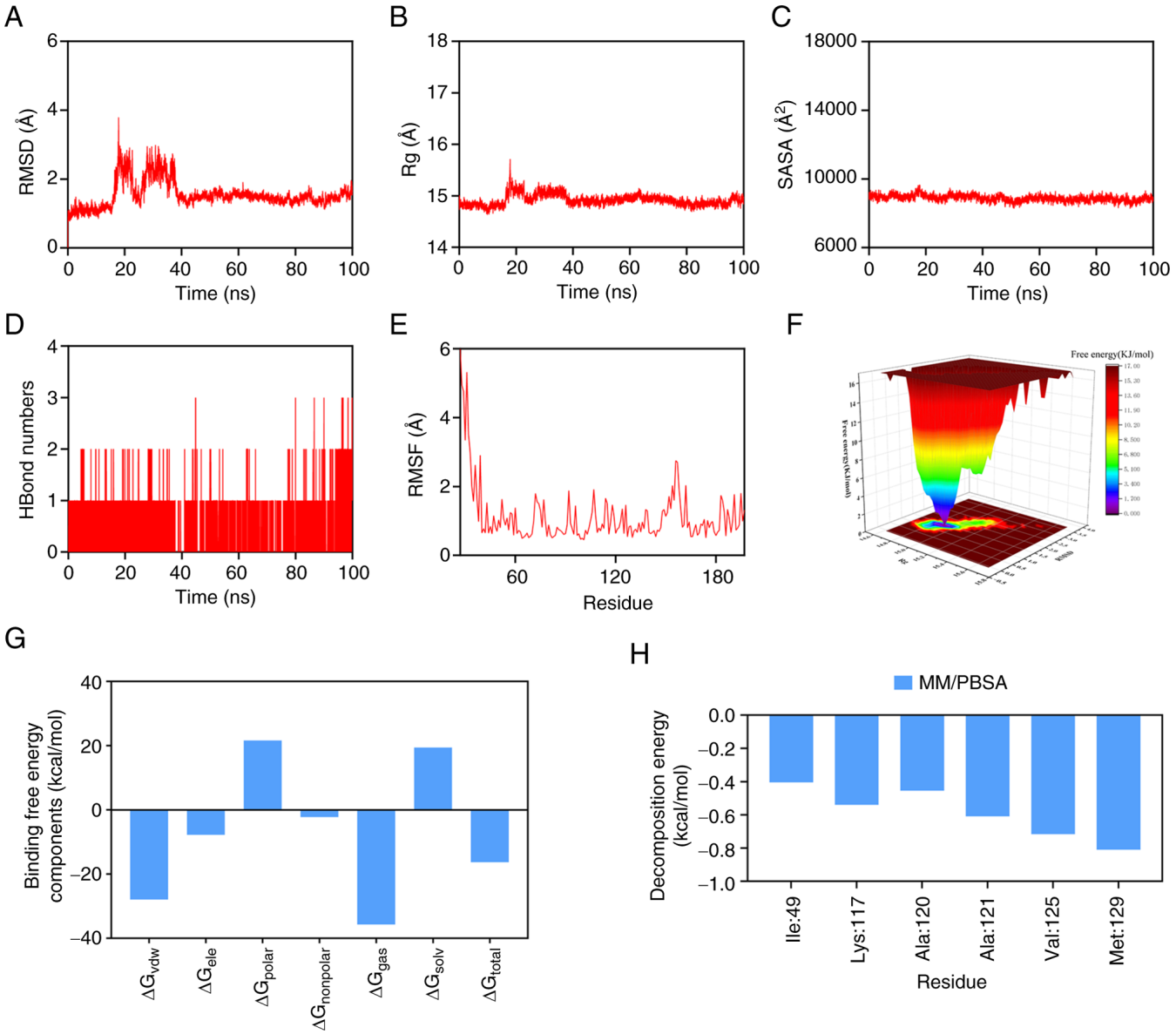

Figure 6. Molecular dynamics analyses of the SC-GPX4 complex. (A) RMSD, (B) Rg, (C) SASA, (D) number of HBonds over time, (E) RMSF by residue, (F) free-energy landscape, (G) binding free-energy components and (H) contributions of key amino acid residues. SC, sanguinarine chloride; GPX4, glutathione peroxidase 4; RMSD, root mean square deviation; Rg, radius of gyration; SASA, solvent-accessible surface area; RMSF, root mean square fluctuation; HBonds, hydrogen bonds; MM/PBSA, Molecular Mechanics Poisson-Boltzmann Surface Area.

detection of apoptotic markers (such as cleaved caspase-3 and Bax/Bcl-2) and specific inhibitors targeting necroptosis or proptosis, are required to dissect the relative contribution and crosstalk between distinct cell death pathways upon SC treatment.

Intracellular ROS accumulation, lipid peroxidation and glutathione depletion are recognized hallmarks of ferroptosis (25,29). MDA is widely used as an indirect indicator of ROS-driven lipid peroxidation and oxidative damage. Consistently, genetic depletion of GPX4 induces ferroptosis accompanied by notable intracellular ROS accumulation (18). In the present study, SC significantly increased lipid ROS and MDA levels and induced characteristic mitochondrial alterations, including increased membrane density and loss of cristae, in liver cancer cells. These findings support a ferroptosis mode of cell death. Despite this, the precise molecular sequence associating SC exposure, GPX4 downregulation and lipid peroxidation remains to be clarified.

Numerous limitations of the present study should be considered. First, although SC significantly reduced GPX4 protein levels, the upstream mechanism remains unknown; specifically, it is unclear whether SC affects GPX4 transcription, translation or protein degradation. Second, molecular docking and MD simulations provide predictive rather than direct evidence of SC-GPX4 binding. Cellular thermal shift assays, drug-affinity responsive target stability assays, surface plasmon resonance or associated biophysical approaches are required to establish direct target engagement. Third, GPX4 overexpression rescue and complementary genetic experiments are needed to further determine the causal role of GPX4 in SC-induced ferroptosis. Finally, the antitumor efficacy and safety of SC should be validated in additional preclinical models.

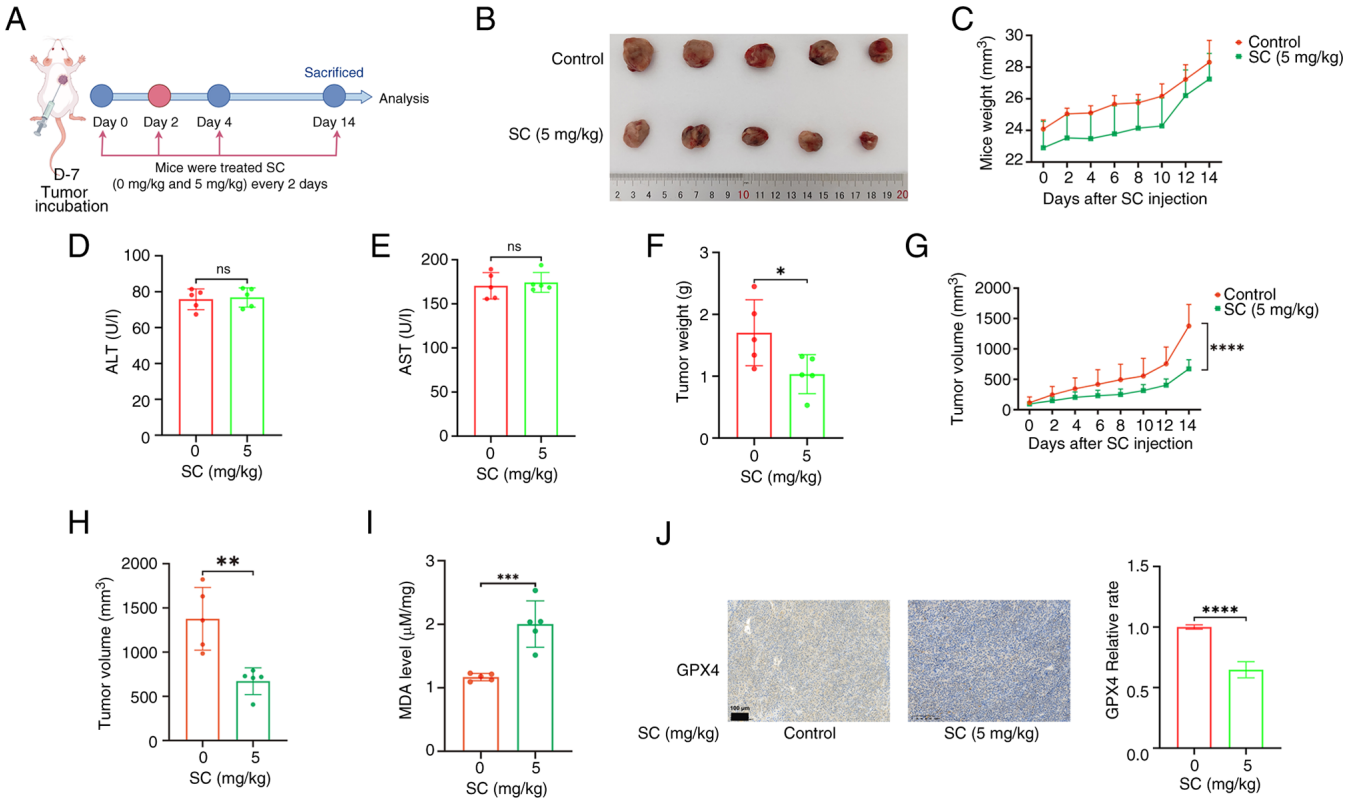

Figure 7. SC suppresses xenograft growth and promotes ferroptosis *in vivo*. (A) Schematic illustration of the subcutaneous xenograft model generated using Figdraw. (B) Representative tumors from the control and SC (5 mg/kg) groups. (C) Body-weight curves. Plasma (D) ALT and (E) AST levels. (F) Tumor weight after 14 days of treatment. (G) Tumor volume after 14 days of treatment. (H) Tumor-growth curves. (I) Tumor MDA levels measured using a commercial kit. (J) Representative IHC staining (left) and quantification (right) of GPX4 expression in tumor tissues. *P<0.05, **P<0.01, ***P<0.001 and ****P<0.0001. SC, sanguinarine chloride; GPX4, glutathione peroxidase 4; MDA, malondialdehyde; AST, aspartate aminotransferase; ALT, alanine aminotransferase; ns, not significant.

In conclusion, SC suppresses liver cancer growth and induces ferroptosis in association with GPX4 downregulation. Further studies are required to verify direct target engagement, define the mechanism by which SC regulates GPX4 and establish its pharmacokinetic, safety and therapeutic profiles before clinical translation.

Acknowledgements

Not applicable.

Funding

The present study was supported by grants from the National Natural Science Foundation of China (grant no. 82201771), the Key Project of Medical Research Fund of Hunan Medical Association (grant no. HMA202101010), the Natural Science Foundation of Hunan Province (grant nos. 2024JJ6083 and 2025JJ50517), the Health Research Project of Hunan Provincial Health Commission (grant no. W20243143), the Natural Science Foundation of Changsha (grant nos. kq2202491 and kq2502316), the Clinical Medical Technology Demonstration Base for Genetic Research of Fetal Congenital Heart Disease in Hunan Province (grant no. 2021SK4036), the Hunan Province Children's Safe Medication Clinical Medical Technology Demonstration Base (grant no. 2023SK4083) and the Open Research Fund of Hunan Provincial Key Laboratory of Regional Hereditary Birth Defects Prevention and Control (grant no. HPKL2023024).

Availability of data and materials

The data generated in the present study may be requested from the corresponding author.

Author's contributions

WYO, JXG and YH contributed to the conception and design of the present study. WYO, JXG and DZ also conducted project administration. Material preparation, data collection and analysis were conducted by JL and LLQ. Data collection and analysis were conducted by BL, YH and DZ. The initial draft of the article was written by WYO. WYO and YH commented on the first and last versions of the article and edited the final version. YH and DZ reviewed and edited the final version of the article. WYO, YH and DZ confirm the authenticity of all the raw data. All authors read and approved the final version of the manuscript.

Ethics approval and consent to participate

All animal experiment protocols were approved by the Ethics Committee for Biomedical Research of Hunan Normal University (approval no. 20250908).

Patient consent for publication

Not applicable.

Competing interests

The authors declare that they have no competing interests.

References

1. Bray F, Laversanne M, Sung H, Ferlay J, Siegel RL, Soerjomataram I and Jemal A: Global cancer statistics 2022: GLOBOCAN estimates of incidence and mortality worldwide for 36 cancers in 185 countries. CA Cancer J Clin 74: 229-263, 2024.
2. Vogel A, Meyer T, Sapisochin G, Salem R and Saborowski A: Hepatocellular carcinoma. Lancet 400: 1345-1362, 2022.
3. Ganesan P and Kulik LM: Hepatocellular carcinoma: New developments. Clin Liver Dis 27: 85-102, 2023.
4. Qin S, Bi F, Gu S, Bai Y, Chen Z, Wang Z, Ying J, Lu Y, Meng Z, Pan H, *et al*: Donafenib versus Sorafenib in first-line treatment of unresectable or metastatic hepatocellular carcinoma: A randomized, open-label, parallel-controlled phase II-III Trial. J Clin Oncol 39: 3002-3011, 2021.
5. Bruix J, Qin S, Merle P, Granito A, Huang YH, Bodoky G, Pracht M, Yokosuka O, Rosmorduc O, Breder V, *et al*: Regorafenib for patients with hepatocellular carcinoma who progressed on sorafenib treatment (RESORCE): A randomised, double-blind, placebo-controlled, phase 3 trial. Lancet 389: 56-66, 2017.
6. Finn RS, Ryoo BY, Hsu CH, Li D, Burgoyne AM, Cotter C, Tamai T, Suzuki T, Hisai T, Hayato S, *et al*: Phase 2 study of lenvatinib in patients with advanced hepatocellular carcinoma. J Gastroenterol 52: 512-519, 2017.
7. Rosen J, Landriscina A, Adler BL, Krauz A, Doerner J, Navati M, Musaev T, Gravekamp C, Nosanchuk J and Friedman AJ: Characterization and assessment of nanoencapsulated sanguinarine chloride as a potential treatment for melanoma. J Drugs Dermatol 14: 453-458, 2015.
8. Xie Y, Zhou X, Li J, Yao XC, Liu WL, Kang FH, Zou ZX, Xu KP, Xu PS and Tan GS: Identification of a new natural biflavonoids against breast cancer cells induced ferroptosis via the mitochondrial pathway. Bioorg Chem 109: 104744, 2021.
9. Alakkal A, Thayyullathil F, Pallichankandy S, Subburayan K, Cheratta AR and Galadari S: Sanguinarine induces H_2O_2-dependent apoptosis and ferroptosis in human cervical cancer. Biomedicines 10: 1795, 2022.
10. Zhong M, Li X, Zhao F, Huang Y, Long Y, Chen K, Tian X, Liu M and Ma X: Natural compound library screening identifies Sanguinarine chloride for the treatment of SCLC by upregulating CDKN1A. Transl Oncol 17: 101345, 2022.
11. Liang X, Cao Y, Duan Z, Wang M, Zhang N, Ding Y, Luo C, Lu N and Chen S: Discovery of new small molecule inhibitors of the BPTF bromodomain. Bioorg Chem 134: 106453, 2023.
12. Yan S, Lin S, Chen K, Yin S, Peng H, Cai N, Ma W, Songyang Z and Huang Y: Natural product library screens identify sanguinarine chloride as a potent inhibitor of telomerase expression and activity. Cells 11: 1485, 2022.
13. Du Y, Wang X, Li C, Jiao L and Hu Y: Effect of Sanguinarine chloride on proliferation and apoptosis of human tongue cancer cells and its mechanism. Panminerva Med 65: 104-106, 2023.
14. Liu S, Tao Y, Wu S, Lin J, Fu S, Lu J, Zhang J, Fu B, Zhang E, Xu J, *et al*: Sanguinarine chloride induces ferroptosis by regulating ROS/BACH1/HMOX1 signaling pathway in prostate cancer. Chin Med 19: 7, 2024.
15. Li B, Cheng K, Wang T, Peng X, Xu P, Liu G, Xue D, Jiao N and Wang C: Research progress on GPX4 targeted compounds. Eur J Med Chem 274: 116548, 2024.
16. Liu YX, Song YS, Liu CK, Liu J, Yu FX, Jiang WS, Liu G, Xu TR and Sang J: *Paris polyphylla* Smith var. yunnanensis-derived saponins potentiate the antitumor activity of GPX4 inhibitors. J Ethnopharmacol 357: 120890, 2025.
17. Lu Y, Wang SS, Li MY, Liu R, Zhu MF, Yang LM, Wang FY, Huang KB and Liang H: Cyclometalated iridium(III) complex based on isoquinoline alkaloid synergistically elicits the ICD response and IDO inhibition via autophagy-dependent ferroptosis. Acta Pharm Sin B 15: 424-437, 2025.
18. Yang WS, SriRamaratnam R, Welsch ME, Shimada K, Skouta R, Viswanathan VS, Cheah JH, Clemons PA, Shamji AF, Clish CB, *et al*: Regulation of ferroptotic cancer cell death by GPX4. Cell 156: 317-331, 2014.
19. Xie Y, Hou W, Song X, Yu Y, Huang J, Sun X, Kang R and Tang D: Ferroptosis: Process and function. Cell Death Differ 23: 369-379, 2016.
20. Li J, Cao F, Yin HL, Huang ZJ, Lin ZT, Mao N, Sun B and Wang G: Ferroptosis: Past, present and future. Cell Death Dis 11: 88, 2020.
21. Chen X, Kang R, Kroemer G and Tang D: Broadening horizons: The role of ferroptosis in cancer. Nat Rev Clin Oncol 18: 280-296, 2021.
22. Wu J, Wang Y, Jiang R, Xue R, Yin X, Wu M and Meng Q: Ferroptosis in liver disease: New insights into disease mechanisms. Cell Death Discov 7: 276, 2021.
23. Wang L, Chen X and Yan C: Ferroptosis: An emerging therapeutic opportunity for cancer, Genes Dis 9: 334-346, 2022.
24. Yang SC, Li B, Zhu YL, Laaksonen A and Wang YL: The ENUF method-Ewald summation based on nonuniform fast Fourier transform: Implementation, parallelization, and application. J Comput Chem 41: 2316-2335, 2020.
25. Liang D, Feng Y, Zandkarimi F, Wang H, Zhang Z, Kim J, Cai Y, Gu W, Stockwell BR and Jiang X: Ferroptosis surveillance independent of GPX4 and differentially regulated by sex hormones. Cell 186: 2748-2764, 2023.
26. Li J, Li Y, Wang D, Liao R and Wu Z: PLAG1 interacts with GPX4 to conquer vulnerability to sorafenib induced ferroptosis through a PVT1/miR-195-5p axis-dependent manner in hepatocellular carcinoma. J Exp Clin Cancer Res 43: 143, 2024.
27. Pei W, Jiang M, Liu H, Song J and Hu J: The prognostic and antitumor roles of key genes of ferroptosis in liver hepatocellular cancer and stomach adenocarcinoma. Cancer Biomark 39: 335-347, 2024.
28. Pan R, Zhao Z, Xu D, Li C and Xia Q: GPX4 transcriptionally promotes hepatocellular carcinoma metastasis via GRHL3/PTEN/PI3K/AKT axis. Transl Res 271: 79-92, 2024.
29. Zhang W, Liu Y, Liao Y, Zhu C and Zou Z: GPX4, ferroptosis, and diseases. Biomed Pharmacother 174: 116512, 2024.
30. Ajoolabady A, Tang D, Kroemer G and Ren J: Ferroptosis in hepatocellular carcinoma: Mechanisms and targeted therapy. Br J Cancer 128: 190-205, 2023.
31. Tang D, Chen X, Kang R and Kroemer G: Ferroptosis: Molecular mechanisms and health implications. Cell Res 31: 107-125, 2021.
32. Kang X, Huo Y, Jia S, He F, Li H, Zhou Q, Chang N, Liu D, Li R, Hu Y, *et al*: Silenced LINC01134 enhances oxaliplatin sensitivity by facilitating ferroptosis through GPX4 in hepatocarcinoma. Front Oncol 12: 939605, 2022.
33. Yao F, Zhou S, Zhang R, Chen Y, Huang W, Yu K, Yang N, Qian X, Tie X, Xu J, *et al*: CRISPR/Cas9 screen reveals that targeting TRIM34 enhances ferroptosis sensitivity and augments immunotherapy efficacy in hepatocellular carcinoma. Cancer Lett 593: 216935, 2024.
34. Yue X, Xiang Z, Yi Y, Wang X, Zhou W, Wu W, Qin W, Zhao Y, Bu X and Peng Z: Targeting the TRIM14/USP14 axis enhances radiotherapy efficacy by inducing GPX4 degradation and disrupting ferroptotic defense in HCC. Cell Death Dis 16: 481, 2025.